Air-Stable Calcium Cyanamide Supported Ruthenium Catalyst for Ammonia Synthesis and Decomposition

Kazuhisa Kishida,[†] *Masaaki Kitano*,[*,†,‡] *Masato Sasase*,[†] *Peter V. Sushko*,[§] *Hitoshi Abe*,[#,‖,⊥]

Yasuhiro Niwa,[#] *Kiya Ogasawara*,[†] *Toshiharu Yokoyama*,[†] *and Hideo Hosono*[*,†]

[†] Materials Research Center for Element Strategy, Tokyo Institute of Technology, 4259 Nagatsuta, Midori-ku, Yokohama 226-8503, Japan

[‡] Precursory Research for Embryonic Science and Technology (PRESTO), Japan Science and Technology Agency (JST), 4-1-8 Honcho, Kawaguchi, Saitama 332-0012, Japan

[§] Physical Sciences Division, Physical & Computational Sciences Directorate, Pacific Northwest National Laboratory, Richland, WA 99352, USA

[#] Institute of Materials Structure Science, High Energy Accelerator Research Organization (KEK), 1-1 Oho, Tsukuba, Ibaraki 305-0801, Japan

[‖] Department of Materials Structure Science, School of High Energy Accelerator Science, SOKENDAI (the Graduate University for Advanced Studies), 1-1 Oho, Tsukuba, Ibaraki 305-0801, Japan

⊥ Graduate School of Science and Technology, Ibaraki University, 2-1-1 Bunkyo, Mito, Ibaraki 310-8512, Japan

KEYWORDS: ammonia synthesis, ammonia decomposition, ruthenium, electride, calcium cyanamide

ABSTRACT: Efficient ammonia synthesis and decomposition processes under mild conditions are important to meet the expanding demand in major application of ammonia as energy carrier as well as to provide feedstock for chemical industry. Here, we report that air-stable calcium cyanamide-supported ruthenium ($Ru/CaCN_2$) works as an efficient and stable catalyst for ammonia synthesis and decomposition. $Ru/CaCN_2$ exhibits greater catalytic performances for both reactions than Ru/Ca_2N electride and Ru-Cs/MgO. The kinetic analysis for ammonia synthesis suggests that $Ru/CaCN_2$ exhibits low apparent activation energy and high resistance to hydrogen poisoning, which has similar characteristics to the kinetic parameters of Ru-supported electride catalyst. H_2-temperature programmed reaction (TPR) and temperature programmed desorption (TPD) revealed that Ru promoted the formation of CN_2 vacancies on $CaCN_2$ surface which in turn capture hydrogen as H^- ions during the reaction. Density functional theory calculations provide insight into how the formation of CN_2 vacancies is promoted by Ru, which leads to the decrease in the work function of $CaCN_2$ surface and the hydrogen capture at the Ru-support interface. These results suggest that the high catalytic performance of $Ru/CaCN_2$ can be attributed to the formation of a quasi-electride structure at Ru-$CaCN_2$ interface.

INTRODUCTION

Ammonia (NH_3) is a ubiquitous precursor for nitrogen-containing chemical products; in recent it also attracted attention as a hydrogen carrier substance.[1] In order to realize more energy-efficient processes for the production of NH_3 and the extraction of H_2 from NH_3, more efficient catalysts for NH_3 synthesis and decomposition at mild conditions are necessary.[2-9] A supported ruthenium (Ru) catalyst with optimum binding energy with nitrogen atom[10-11] is one of the most promising catalysts for these reactions.[12-13] It is widely accepted that cleavage of the N≡N triple bond and the recombinative desorption of nitrogen adatoms from the catalyst surface are the rate-determining steps for NH_3 synthesis[14] and decomposition,[15] respectively. In the attempt to accelerate these rate-determining steps, the modification of supported Ru catalysts with alkali promoters (K, Cs, or Ba hydroxide or oxides) has greatly contributed to the progress by its electronic promotion effect.[16-22] It has been generally recognized that the role of alkali promoters in NH_3 synthesis is to inject electrons to the antibonding π^*-orbital of adsorbed N_2 molecule via Ru.[23-24] However, these nitrogen activation steps on Ru surface are suppressed by H_2 poisoning because of high affinity of Ru to H_2.

We have previously demonstrated that $12CaO \cdot 7Al_2O_3$ electride (C12A7:e^-) significantly enhances the activity of Ru catalysts in both NH_3 synthesis and decomposition.[25-26] The C12A7:e^- contains high density anionic electrons in the subnanometer-sized cages with positive charge, which results in high electrical conductivity as well as low work function (2.4 eV).[27] Accordingly, the electronic promotion effect of this material is much higher than that of a conventional promoter, such as Cs in Cs-loaded metal oxide. In addition, reversible hydrogen capture-release capability of C12A7:e^- can prevent the H_2 poisoning over Ru surface.

Ru/C12A7:e^- catalyst exhibits low apparent activation energy (50–65 kJ mol^{-1}) and positive reaction order for H_2 in both NH_3 synthesis and decomposition.[25-26]

Recently, the electronic signatures of electride-like behavior have also been observed in some ionic compounds such as CaH_2[28-29] and $Ca(NH_2)_2$.[30-31] When these materials are used as support for Ru catalysts, anionic electrons are formed at the anion vacancies on the Ru-support interface during catalytic reaction, resulting in a low work function (2.1–2.7 eV). These catalysts surpass the activity of Ru/C12A7:e^- for both reactions. However, these compounds are difficult to handle in air because of their sensitivity to air and moisture.

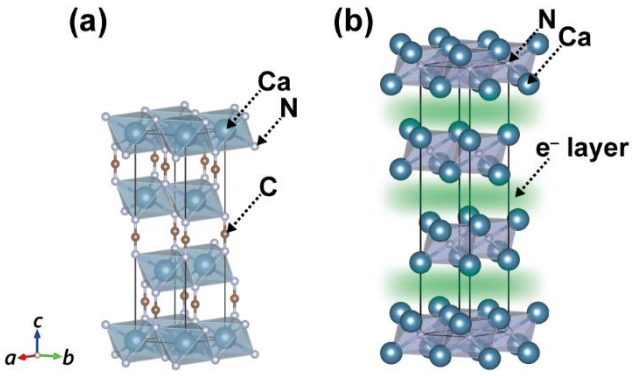

Figure 1. Crystal structures of (a) $CaCN_2$ (R-3m space group) and (b) Ca_2N:e^- (R-3m space group). The crystal structures were pictured with the VESTA program.[32]

Here, we report that an air-stable ionic compound, calcium cyanamide ($CaCN_2$), enhances the activity of Ru catalysts in NH_3 synthesis and decomposition at mild conditions. $CaCN_2$ is well-known as a main component of lime nitrogen, which has been used as a nitrogen-based fertilizer since the early 20th century. Interestingly, as shown in Figure 1, the crystal structure of $CaCN_2$ is quite similar to that of a two-dimensional electride, $[Ca_2N]^+ \cdot e^-$ (Ca_2N:e^-).[33] Ru/Ca_2N:e^-

functions as an efficient catalyst for NH_3 synthesis at mild conditions[28] but it is unstable in air due to low resistivity of $Ca_2N{:}e^-$ to oxygen and moisure.[33] In contrast, $Ru/CaCN_2$ works as an efficient catalyst for both NH_3 synthesis and decomposition even after exposure to air. Experimental and theoretical investigation reveals that anionic electrons with low work function are created in the CN_2 vacancy during catalytic reaction. The surface electride formation on $CaCN_2$ promotes the NH_3 synthesis and decomposition over Ru catalyst.

EXPERIMENTAL SECTION

Catalyst preparation. To synthesize $CaCN_2$, $CaCO_3$ (Kojundo chemical laboratory, 99.99%) was heated in a vertical silica tube furnace under an NH_3 gas flow (100 mL min^{-1}) at 550 ℃ for 20 h. To prepare the Ru-loaded sample, the $CaCN_2$ powder and $Ru_3(CO)_{12}$ (Sigma-Aldrich, 99%) were mixed using agate mortar. The mixture was sealed in an evacuated silica tube and then heated according to the method reported previously.[25] The procedures to prepare reference catalysts are described in the Supporting Information.

Catalytic reactions. Catalytic reactions were conducted in a fixed-bed continuous-flow straight tube reactor. Prior to the NH_3 synthesis and decomposition reactions, the catalysts were activated in situ by reducing Ru metal under a H_2 gas flow (10 mL min^{-1}) at 340 ℃ for 20 min ($Ru/CaCN_2$) or under a N_2/H_2 mixed gas flow ($N_2{:}H_2$ = 1:3, 60 mL min^{-1}) at 340 ℃ for 20 min (for $Ru/Ca_2N{:}e^-$) or at 400 °C for 1 h (for Ru-Cs/MgO, Ru/MgO and $Ru/\gamma\text{-}Al_2O_3$).

NH_3 synthesis activities were evaluated using 100 mg of catalyst in a silica glass or stainless-steel reactor at a temperature range of 220–400 ℃, 0.1 or 0.9 MPa and a N_2/H_2 mixed gas flow ($N_2{:}H_2$ = 1:3, 60 mL min^{-1}) which corresponds to a weight hourly space velocity (WHSV) of

36000 mL g_{cat}^{-1} h^{-1}. The NH_3 produced was trapped by in 5 mM sulfuric acid solution and the amount of NH_4^+ generated in the solution was determined using ion chromatography (LC-2000 plus, Jasco).

The kinetic analysis of 5 wt% Ru/$CaCN_2$ was performed in a similar manner to the previously reported procedure.[34] The reaction orders with respect to N_2 and H_2 were established by using mixed gas (N_2 10.0–33.3 vol%, H_2 33.3–66.7 vol% and Ar balance) at a flow rate of 60 mL min^{-1}. The reaction orders with respect to NH_3 were established by changing the flow rate of N_2/H_2 mixed gas (N_2:H_2 = 1:3, 30–60 mL min^{-1}). All kinetic experiments were conducted at 300 °C and 0.1 MPa far from equilibrium conditions (for example, the conversion level was less than 30% of that at equilibrium). The reaction orders were estimated by using Eqs. (1)–(5).

$$r = kP_{N_2}^{\alpha} P_{H_2}^{\beta} P_{NH_3}^{\gamma} \quad (1)$$

$$r = \left(\frac{1}{W}\right) \frac{\mathrm{d}y_0}{\mathrm{d}(1/q)} \quad (2)$$

$$\log y_0 = \log \left(\frac{C}{q}\right)^{\frac{1}{m}} \quad (3)$$

$$r = \left(\frac{1}{W}\right) \left(\frac{C}{m}\right) y_0^{(1-m)} \quad (4)$$

$$C = k_2 P_{N_2}^{\alpha} P_{H_2}^{\beta} \quad (5)$$

Here, r, W, y_0, q, and $(1-m)$ denote the NH_3 synthesis rate, the weight of catalyst, the concentration of NH_3 in the outlet gas, the total gas flow rate, and the reaction order for NH_3 (γ). The reaction order for N_2 (α) and H_2 (β) can be determined by plotting the logarithm of constant "C" vs that of partial pressure of N_2 or H_2.

NH_3 synthesis using $^{15}N_2$ and H_2 was conducted at 400 °C over 5 wt% $Ru/CaCN_2$ (0.2 g) in a U-shaped glass reactor connected to a closed gas circulation system. Prior to the reaction, the catalyst was pretreated at 340 °C for 20 min under a H_2 gas flow (10 mL min^{-1}) and then at 340 °C for 24 h under a N_2/H_2 mixed gas flow (N_2:H_2 = 1:3, 60 mL min^{-1}) in a fixed-bed, continuous-flow, straight, silica-glass tube reactor. A mixture of $^{15}N_2$ (98%+ as $^{15}N_2$, Cambridge Isotope Laboratories Inc., USA) and H_2 gases (total pressure: 60 kPa, $^{15}N_2$:H_2 = 1:3) was introduced into the glass system. The change in the composition of the circulating gas was monitored with a quadrupole mass spectrometer (M-101QA-TDM, Canon Anelva Corp.), and Ar was used as carrier gas. The m/z = 2, 16, 17, 18, 28, 29, and 30 signals were monitored as a function of time to follow the reaction.

NH_3 decomposition activities were evaluated using 60 mg of catalyst in a silica glass reactor at a temperature range of 200–400 °C, a pure NH_3 gas flow rate of 15 mL min^{-1} which corresponds to a WHSV of 15000 mL_{NH3} g_{cat}^{-1} h^{-1}. Effluent gases were analyzed using an online gas chromatograph (GC-14A, TCD, Porapak QS and molecular sieve 5A columns, Shimadzu; He carrier gas). The calculation of NH_3 conversion X_{NH3} [%] was calculated by Eq. (6), taking into account the change in the total volume of the gas phase under constant reaction temperature and total pressure in a plug-flow system.[35]

$$X_{\mathrm{NH_3}} = \frac{C_{NH_3,0} - C_{NH_3}}{C_{NH_3,0} + C_{NH_3}} \times 100 \qquad (6)$$

Where $C_{NH3,0}$ is the concentration of NH_3 in the inlet gas, C_{NH3} is the concentration of NH_3 in the outlet gas [mol m^{-3}].

Characterization. X-ray diffraction (XRD) patterns were recorded on a Bruker D8 Advance diffractometer using monochromatic Cu$K\alpha$ radiation (λ = 0.15418 nm) at 45 kV and 360 mA.

Specific surface areas were calculated using the Brunauer-Emmet-Teller (BET) multipoint method from N_2 adsorption isotherms at 77 K with a MicrotracBEL BELSORP-mini II. H_2-temperature programmed reaction (TPR) and temperature programmed desorption (TPD) were conducted in a fixed-bed continuous-flow straight tube reactor. Prior to the analyses, 2 wt% $Ru/CaCN_2$ (30 mg) was activated under a H_2 gas flow (5 mL min^{-1}) at 340 °C and 0.1 MPa for 20 min. TPR analysis was carried out by heating the catalyst under an H_2 gas flow (5 mL min^{-1}) from room temperature to 400 ℃ at a heating rate of 3.33 ℃ min^{-1}. The outlet gas was monitored using a quadrupole mass spectrometer (M-101QA-TDM, Canon Anelva Corp.), and Ar was used as carrier gas. The m/z = 2, 15, 17, 27, and 28 signals were monitored as a function of time to monitor the reaction. H_2-TPD for $Ru/CaCN_2$ after reaction was carried out using a MicrotracBEL BELCAT-A catalyst analyzer. Prior to the analysis, 5 wt% $Ru/CaCN_2$ (100 mg) was activated under a H_2 gas flow (10 mL min^{-1}) at 340 ℃ for 20 min and then heated under N_2/H_2 mixed gas flow (N_2:H_2 = 1:3, 60 mL min^{-1}) at 340 ℃ and 0.1 MPa for 20 h in a straight silica glass tube reactor. The catalyst (65 mg) was transferred to a TPD glass reactor in an Ar-filled glovebox. Next, the catalyst in the reactor attached to the catalyst analyzer was heated under an Ar gas flow (10 mL min^{-1}) at 40 ℃ for 5 min. Thereafter, TPD analysis was carried out by heating the catalyst under an Ar gas flow (50 mL min^{-1}) from 50 to 1000 °C at a heating rate of 10 ℃ min^{-1}. The outlet gas was monitored using mass spectrometry (Bell Mass, MicrotracBEL, Japan). High-angle annular dark-field scanning transmission electron microscopy (HAADF-STEM) images were obtained using a JEOL JEM-ARM200F atomic resolution analytical electron microscope operated at an accelerating voltage of 200 kV. The samples for STEM observation were prepared by putting a drop of catalyst suspension dispersed in *n*-hexane on an amorphous carbon film-coated copper microgrid and drying it in an Ar atmosphere at room

temperature. The average Ru particle size was obtained by measuring diameters of more than 300 Ru particles imaged using STEM, according to the method described elsewhere.[36] X-ray absorption fine structure (XAFS) experiments were carried out at the NW10A beamline of the Photon Factory at KEK (Proposal No. 2013S2-002). A Si(311) double-crystal monochromator was used to obtain the monochromated X-ray beam, and the Ru K edge spectra were recorded at room temperature in the transmission mode. The XAFS spectra were analyzed by using the Athena and Artemis software packages[37] and the FEFF6 code.[38]

Calculations. Stoichiometric $CaCN_2$ was represented using a symmetric periodic slab model and an orthorhombic supercell containing four full Ca^{2+} layers and three full CN_2^{2-} layers; the outer Ca^{2+} layers were covered with an additional 0.5 monolayer of CN_2^{2-} (see Figure S1a). The lateral cell parameters were fixed at the experimental values a = 7.3137 Å and b = 6.3367 Å. The period in the direction perpendicular to the slab was fixed at a = 50 Å, which ensures at least 20 Å wide vacuum gap. Symmetric slab was used for the calculations of the work function and one-electron densities of states (DOS). The relative stabilities of transient configurations along the proposed reaction pathways were considered on one slab surface only.

The simulations were conducted using the Vienna Ab initio Simulation Package (VASP).[39-40] The projector-augmented wave potentials were used to approximate the effect of the core electrons.[41] We used the Perdew-Burke-Ernzerhof generalized gradient approximation density functional modified for solids (PBEsol).[42] Internal degrees of freedom were fully relaxed. A gamma-centered 4×4×1 k-mesh was used for Brillouin-zone integration for the structure optimizations, 8×8×1 k-mesh was used for subsequent DOS calculations. The plane-wave basis-set cutoff was set to 500 eV. Reaction barriers were calculated using climbing-image nudged

elastic band method as implemented in VAPS. For this purpose 2×2×1 k-mesh was reduced. The work function was defined as the difference between the Fermi energy of the slab and the electrostatic potential in the vacuum gap of the supercell (see Figure S1b). Binding energies were calculated with respect to gas phase molecules H_2, N_2, and CH_4.

RESULTS AND DISCUSSION

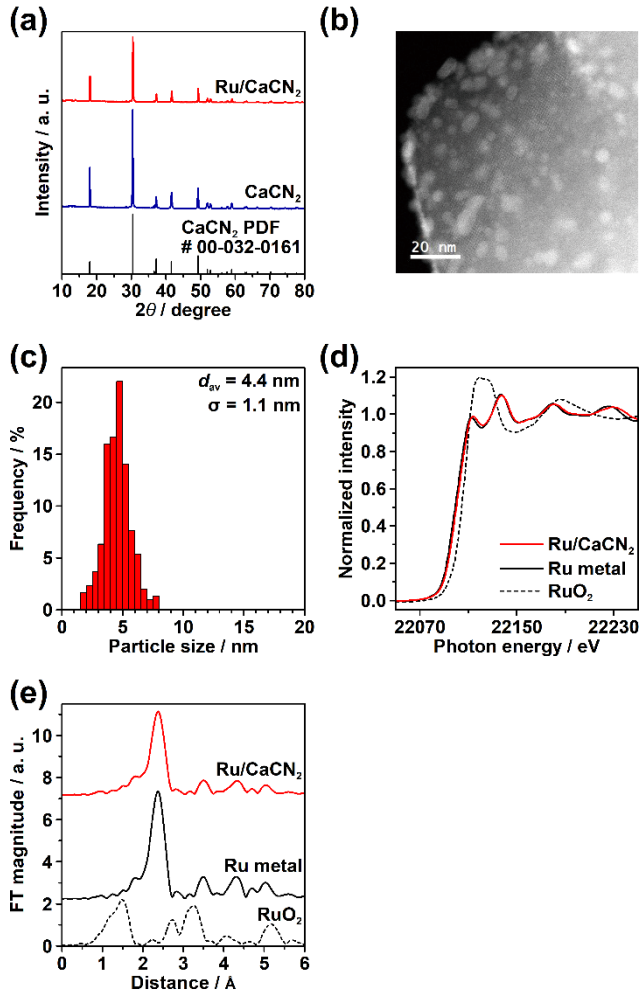

Figure 2. (a) XRD patterns of $CaCN_2$ and 5 wt% Ru/$CaCN_2$ and reference XRD pattern of $CaCN_2$. (b) Representative HAADF-STEM image of 5 wt% Ru/$CaCN_2$ after NH_3 synthesis. (c) Histogram

of the size distributions of Ru particles for 5 wt% Ru/$CaCN_2$ after NH_3 synthesis. (d) Ru *K*-edge XANES spectra of 5 wt% Ru/$CaCN_2$, Ru foil and RuO_2. (e) Fourier transforms of EXAFS oscillations of 5 wt% Ru/$CaCN_2$, Ru foil and RuO_2.

From the X-ray diffraction (XRD) pattern of Ru/$CaCN_2$ (Figure 2a), no diffraction peaks other than those of trigonal $CaCN_2$ was detected, which implies that small-sized Ru nanoparticles (NPs) are dispersed on the surface of $CaCN_2$. Ru NPs with irregular morphology were observed by a representative HAADF-STEM image of Ru/$CaCN_2$ (Figure 2b). The size of Ru NPs is in the range of 1.5–8.0 nm with average particle size of 4.4 nm (Figure 2c). The optimum Ru particle size for NH_3 synthesis and decomposition is reported to be 1.8–2.5 nm because the density of active sites (B_5 step site) reaches maximum at ~2 nm.[43] In the case of Ru/$CaCN_2$, only 4% of Ru NPs are in this narrow range. The Ru *K*-edge X-ray absorption near-edge structure (XANES) spectra showed that the edge position of Ru/$CaCN_2$ is identical to that of Ru foil, which suggests that the chemical state of Ru NPs on $CaCN_2$ are metallic (Figure 2d). The Fourier transforms (FTs) of the extended X-ray absorption fine structure (EXAFS) oscillation of Ru/$CaCN_2$ showed a peak corresponding to Ru−Ru bond at 2.3 Å (Figure 2e). The Ru−Ru bond is consistent with that for the bulk Ru metal. The other peaks derived from Ru-support interaction such as Ru-C and Ru-N were not observed.

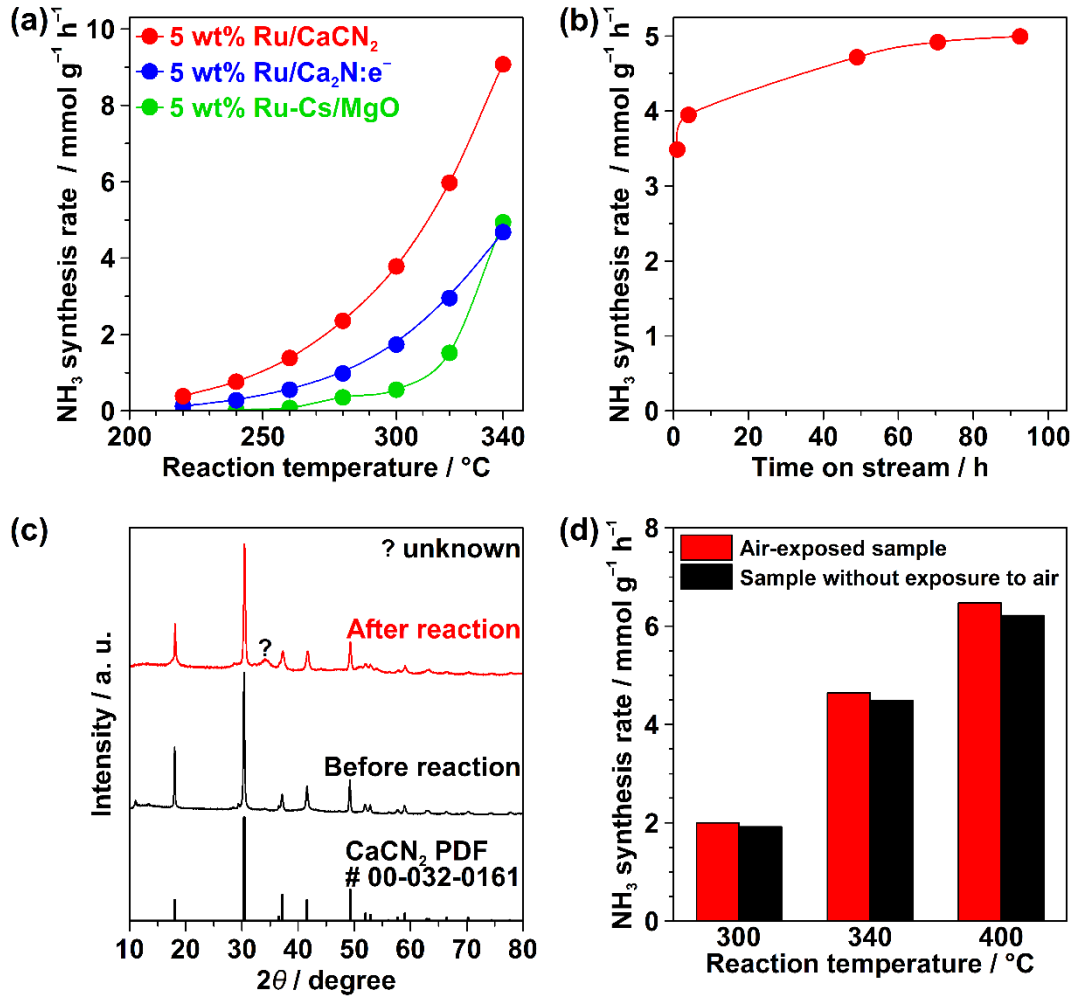

Figure 3. (a) Temperature dependence on NH_3 synthesis rate of 5 wt% Ru catalysts at 0.9 MPa (reaction conditions: catalyst 100 mg; WHSV 36000 mL g_{cat}^{-1} h^{-1}). (b) Time course of NH_3 synthesis over 2 wt% $Ru/CaCN_2$ at 400 °C and 0.1 MPa (reaction conditions: catalyst 100 mg; WHSV 36000 mL g_{cat}^{-1} h^{-1}). (c) XRD patterns of 2 wt% $Ru/CaCN_2$ before and after the NH_3 synthesis at 400 °C and 0.1 MPa for 96 h and reference XRD pattern of $CaCN_2$. (d) NH_3 synthesis rate of 5 wt% $Ru/CaCN_2$ with and without exposure to air before NH_3 synthesis reaction. (reaction conditions: catalyst 100 mg; pressure 0.1 MPa; WHSV 36000 mL g_{cat}^{-1} h^{-1}). For the sample without exposure to air, it was treated in an argon-filled glovebox with O_2 and H_2O content below 1 ppm.

Figure 3a shows temperature dependence on NH_3 synthesis rate of $Ru/CaCN_2$, $Ru/Ca_2N{:}e^-$ and Ru-Cs/MgO at 0.9 MPa. $Ru/CaCN_2$ exhibited higher activity than $Ru/Ca_2N{:}e^-$ and Ru-Cs/MgO in the temperature range of 220–340 °C. In addition, the NH_3 synthesis rate of $Ru/CaCN_2$ did not decrease over 90 h (Figure 3b) and there was no significant change in the crystal structure of $CaCN_2$ before and after the reaction (Figure 3c), which shows that $Ru/CaCN_2$ is a stable catalyst for NH_3 synthesis. The total amount of NH_3 (32.5 mmol, based on initial NH_3 synthesis rate) produced during the stability test is much larger than what (2.45 mmol) can be generated by the decomposition of $CaCN_2$ (98 mg) with H_2 gas. This result clearly shows that the formation of NH_3 is due to catalytic dissociation and hydrogenation of gaseous N_2 molecule over $Ru/CaCN_2$ rather than $CaCN_2$ decomposition. Furthermore, it was confirmed that the catalytic performance of $Ru/CaCN_2$ is not influenced with or without exposure to air (Figure 3d). Additionally, the crystal structure of $Ru/CaCN_2$ without exposure to air (Figure S4) is almost identical to that of air-exposed samples (Figures 2c). These results clearly indicate high tolerance of $Ru/CaCN_2$ to air and moisture.

Table 1. Catalytic performance on various supports for NH_3 synthesis at 300 °C and 0.9 MPa.

Catalyst	S. S. A.[a] / $m^2\ g^{-1}$	Ru particle size[b] / nm	Ru dispersion[b] / %	NH_3 synthesis rate[d] / μmol $g^{-1}\ h^{-1}$	TOF[d] ($\times 10^3$) / s^{-1}	E_a[e] / kJ mol^{-1}
5 wt% $Ru/CaCN_2$	6.8	4.4	29.7	3785	7.3	63.5
5 wt% $Ru/Ca_2N{:}e^-$	5.3	6.6	19.9	1740	5.0	73.4
5 wt% Ru-Cs/MgO	23.6	2.6[c]	50.9[c]	553	0.6	125.4

[a]S. S. A. = specific surface area. [b]These values were estimated by averaging the particle sizes measured by STEM. [c]From ref. 44. [d]Reaction conditions: catalyst 100 mg; temperature 300 °C; mixed gas 60 mL min^{-1} (H_2/N_2 = 3); weight hourly space velocity (WHSV) 36000 mL g_{cat}^{-1} h^{-1}; pressure 0.9 MPa. [e]The apparent activation energy E_a was calculated from Arrhenius plots for the NH_3 synthesis rate in the temperature range of 280–340 °C.

Table 1 summarizes catalytic properties of $Ru/CaCN_2$, $Ru/Ca_2N:e^-$ and Ru-Cs/MgO for NH_3 synthesis at 300 °C and 0.9 MPa. As for NH_3 synthesis rate, $Ru/CaCN_2$ showed two and seven times higher activity than $Ru/Ca_2N:e^-$ and Ru-Cs/MgO, respectively. The turnover frequency (TOF) of $Ru/CaCN_2$ was an order of magnitude higher than that of Ru-Cs/MgO and was comparable to that of $Ru/Ca_2N:e^-$, which means that $CaCN_2$ support has a high electron donating ability, comparable to that of $Ca_2N:e^-$, which has a very low work function (2.6 eV). The higher NH_3 synthesis rate of $Ru/CaCN_2$ than that of $Ru/Ca_2N:e^-$ is attributed to smaller Ru particle size of $Ru/CaCN_2$ (Figure S5). Ru NPs were well dispersed on $CaCN_2$ support with higher surface area (6.4 m^2 g^{-1}) than that (2.1 m^2 g^{-1}) on $Ca_2N:e^-$ support. The apparent activation energy (E_a) of $Ru/CaCN_2$ for NH_3 synthesis was 63.5 kJ mol^{-1} (Table 1 and Figure S6). The value was slightly lower than that of $Ru/Ca_2N:e^-$ (73.4 kJ mol^{-1}) and almost half of that of Ru-Cs/MgO (125.4 kJ mol^{-1}). Furthermore, the E_a of $Ru/CaCN_2$ is close to those (50–65 kJ mol^{-1}) of the electride-supported Ru catalysts, Ru/CaH_2 and $Ru/Ca(NH_2)_2$ reported previously.[25, 28, 30-31, 45-49] The catalytic performance of $Ru/CaCN_2$ is far inferior to those of $Ru/Ba\text{-}Ca(NH_2)_2$[31] and $Ru/Ba/LaCeO_x$[19] but is comparable to other recently reported catalysts including electrides and hydrides, most of which are difficult to handle in air (Table S1). We conclude that air-stable $CaCN_2$ functions as an excellent support for Ru catalyst with high electronic promotion ability, similar to that of other electride-supports, enabling efficient NH_3 synthesis.

Kinetic analysis was conducted at 300 ℃ and 0.1 MPa to clarify the reaction mechanism for NH_3 synthesis over $Ru/CaCN_2$ (Figure S7 and Table S2). As for the reaction order for N_2 and H_2, $Ru/CaCN_2$ showed 0.82 and –0.03, respectively. In general, conventional Ru catalysts show a large negative value ($\beta \leq -0.5$) for H_2 reaction order at lower temperatures (≤ 400 °C).[50] The reaction order of $Ru/CaCN_2$ for H_2 is close to zero at 300 °C, which is slightly more positive than that of Ru/C12A7:e^- ($\beta = -0.16$ at 300 °C) with high tolerance to H_2 poisoning.[51] This result implies that $CaCN_2$ support can transiently capture and release hydrogen during the NH_3 synthesis process, which prevents H_2 poisoning on Ru at low reaction temperature.

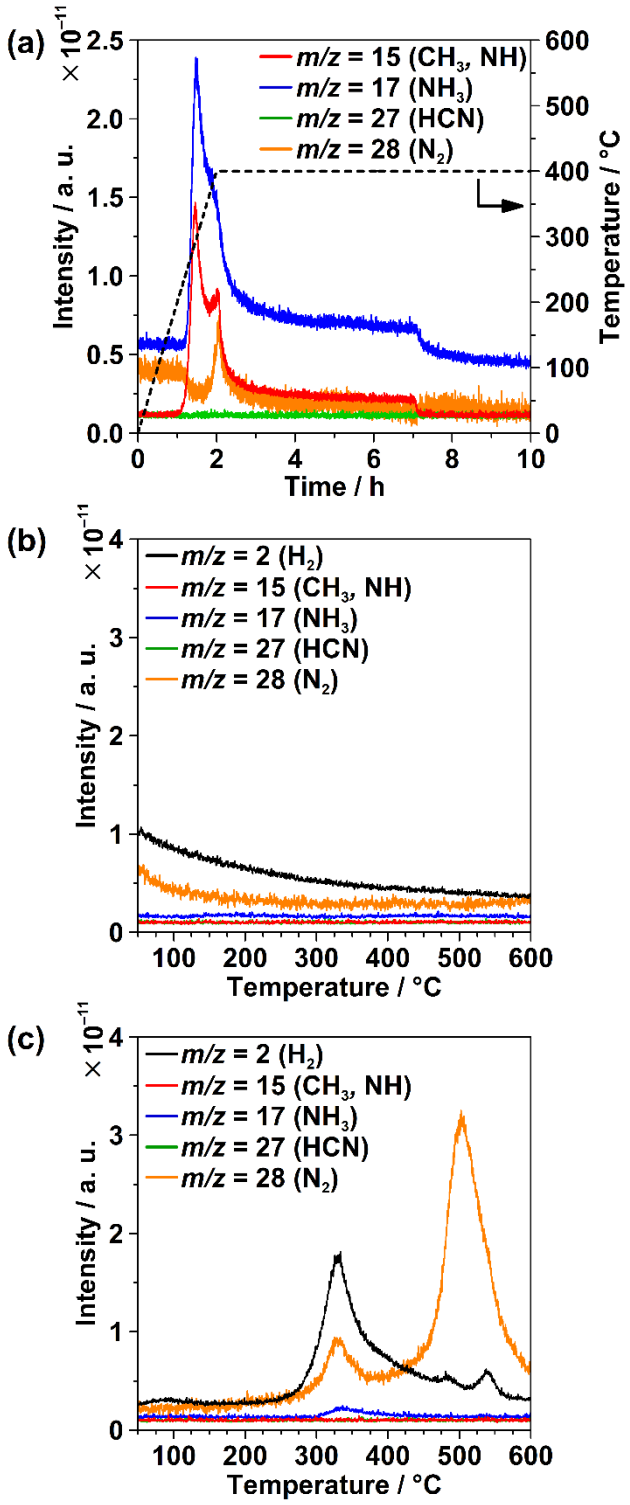

Figure 4. (a) H_2-TPR profiles (m/z = 15, 17, 27, and 28) for 2 wt% Ru/$CaCN_2$. TPD profiles (m/z = 2, 15, 17, 27, and 28) for (b) $CaCN_2$ and (c) 2 wt% Ru/$CaCN_2$ after pretreatment.

To elucidate the contribution of the $CaCN_2$ support to the reaction mechanism of NH_3 synthesis, H_2-TPR and TPD analyses were performed on the Ru/$CaCN_2$. In the H_2-TPR profiles of Ru/$CaCN_2$ (Figure 4a), mass signals with m/z = 15, 17, and 28 were confirmed above 200 °C and disappeared after holding at 400 °C for 5 h. The signal with m/z = 15 is attributed to CH_3 (a fragment of CH_4) and NH (a fragment of NH_3), m/z = 17 and 28 are due to NH_3 and N_2, respectively, which are derived from the hydrogenation of CN_2 species. This suggests that $CaCN_2$ is partially decomposed to form CN_2 vacancy on the surface during NH_3 synthesis. TPD measurements (Figure 4b,c) revealed that no gas desorption was observed from Ru-free $CaCN_2$, whereas H_2, N_2, and NH_3 were desorbed from Ru/$CaCN_2$ above 230 °C. This suggests that Ru promotes the formation of CN_2 vacancies on the $CaCN_2$ surface and a part of CN_2 vacancies are occupied by hydrogen species. In the H_2-TPD profile of Ru/$CaCN_2$ after NH_3 synthesis (Figure S8), the total amount of H_2 desorbed from the catalyst is estimated to be 0.28 mmol g_{cat}^{-1}, which is twice as much as the amount of hydrogen species on Ru surface with a stoichiometry of H/Ru = 1 (0.14 mmol g_{cat}^{-1}). This implies that hydrogen desorption (Figure S8) stems not only from hydrogen adatoms on the Ru surface but also from hydrogen species incorporated in the CN_2 vacancies at Ru-$CaCN_2$ interface. From these results, it can be considered that a part of hydrogen on Ru surface spill over onto $CaCN_2$ support and is incorporated into the CN_2 vacancies of Ru-$CaCN_2$ interfaces as H^- ions, which is consistent with high tolerance to H_2 poisoning in analogous to electride-based catalysts.[25, 28, 45-49, 51] In turn, the existence of CN_2 vacancies is indicative of the formation of a quasi-electride structure near the surface of the $CaCN_2$ support.

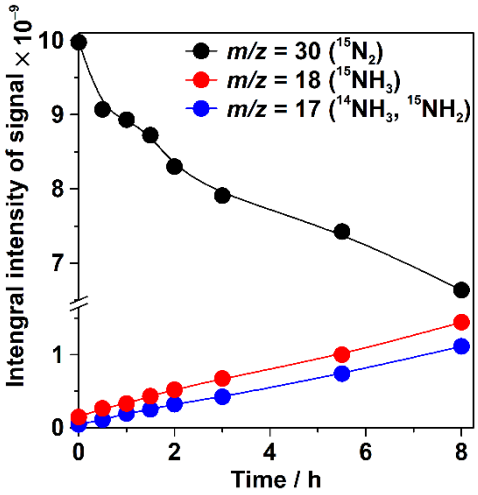

Figure 5. Reaction time profiles for NH_3 synthesis from $^{15}N_2$ and H_2 over 5 wt% $Ru/CaCN_2$. (Reaction conditions: catalyst, 0.2 g; reaction temperature, 400 ºC; reaction gas, $^{15}N_2$:H_2 = 1:3; reaction pressure, 60 kPa).

To further investigate the reaction mechanism of NH_3 synthesis over $Ru/CaCN_2$, NH_3 synthesis using isotopic $^{15}N_2$ and H_2 was conducted (Figure 5). The mass signals with *m*/*z* = 18 ($^{15}NH_3$) and 17 [$^{15}NH_2$ (a fragment of $^{15}NH_3$)] increased with reaction time. The intensity ratio of *m*/*z* = 18 to 17 was approximately 0.77, which is very close to the theoretical value (NH_2/NH_3 = 0.8) for NH_3 molecule, suggesting that these signals originate from $^{15}NH_3$. This conclusion is very similar to the case for isotopic NH_3 synthesis over $Ru/Ba\text{-}Ca(NH_2)_2$,[31] where lattice nitrogen does not participate in the NH_3 synthesis reaction. It was thus demonstrated that NH_3 formation over $Ru/CaCN_2$ proceeds through an electronic promoted N_2 activation rather than lattice nitrogen mediated Mars-van Krevelen mechanism.[52]

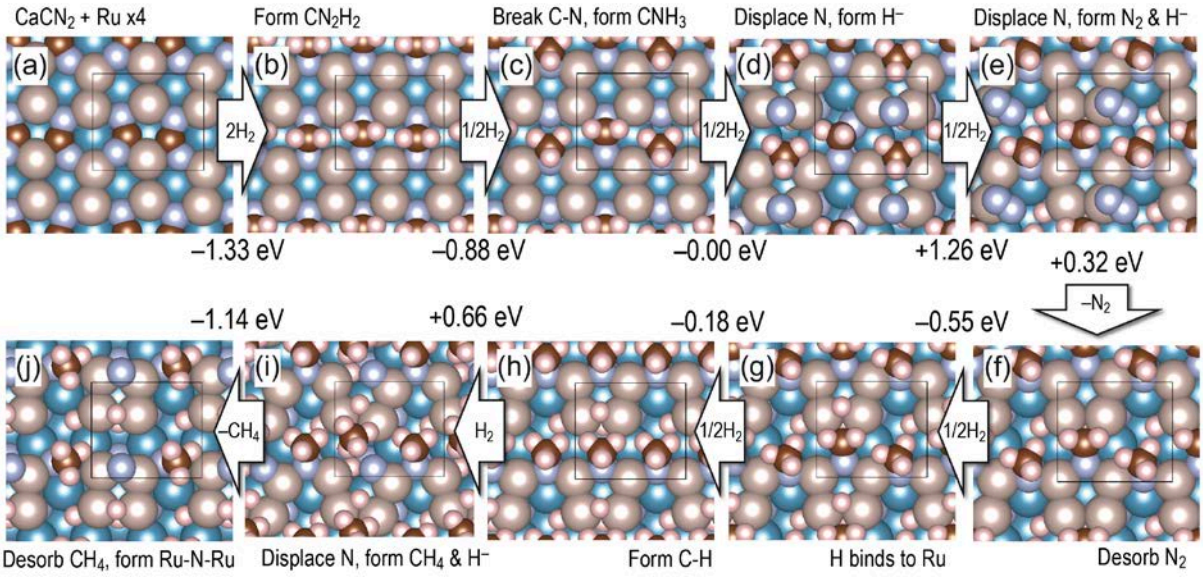

Figure 6. Elementary steps of H_2 interaction with Ru/$CaCN_2$ surface leading to decomposition of the surface CN_2 species: (a) adsorption of Ru atoms; (b) dissociative adsorption of H_2, formation of CN_2H_2; (c,d) adsorption and heterolytic splitting of H_2: H^+ breaks C-N and forms C-H bond (i.e., formation of CNH_3) accompanied by the formation of subsurface H^- and displacement of N into an adatom site; (e) adsorption of $1/2H_2$ leading to incorporation of H^- at the Ru/Ca interface displacement of N to the adatom site with the formation of N_2; (f) desorption of N_2; (g,h) adsorption of H_2, formation of an additional CNH_3 and H adsorbed on Ru; (i) adsorption on heterolytic splitting of H_2: H^+ breaks C-N and converts it to CH_4, H^- replaces N into the adatom site; (j) CH_4 desorbs and Ru cluster restructures to accommodate for the rearrangement of Ru-N bonds. We considered H_2 gas as a source of hydrogen species at the Ru/$CaCN_2$ surface; one half of the energy of a gas-phase H_2 was used as the reference energy for H. Rectangular box in each image marks the lateral cell used in the simulations.

Electronic and chemical properties of $CaCN_2$ were analyzed using density functional theory (DFT) calculations. The work functions (WF) of $CaCN_2$ with CN_2 vacancies (V_{CN2}) at the surface and in the subsurface region were determined to be ca. 3.95 and 3.8 eV, respectively.

While these WF values are higher than those of C12A7:e^- (2.4 eV) and Ca_2N:e^- (2.6 eV) electrides, we find that does not diminish the ability of reduced $CaCN_2$ to transfer the electron charge to the adsorbed Ru particles. Furthermore, we find that surface V_{CN2} can be formed by annealing Ru/$CaCN_2$ system in the presence of hydrogen, thus providing excess electrons that enhance Ru catalytic activity.

Stoichiometric $CaCN_2$ was modelled using a periodic slab terminated with $[CN_2]^{2-}$ ions at 50% coverage density (see Fig. S1 in Supporting method). Deposition of Ru atoms on this surface (see Fig. S2) leads to a gradual elongation of the Ca–N bonds from 2.58 to 3.11 Å on average and the formation of the Ru–N bonds instead. Simultaneously, C–N bond lengths in CN_2^{2-} anions elongate as well (from 1.24 to 1.36 Å), leaving the central C atom exposed to reactions with other chemical species.

Here we consider CN_2 decomposition in the vicinity of low-coordinated Ru atoms that mimic fringes of Ru particles. Such model captures the key interactions, including strain induced by the formation of Ru–N bonds, and allows for the desorption of the CN_2 decomposition products. It also allows for charge disproportionation among the Ru atoms in the presence of the ionic substrate. Elementary steps leading to the activation of the Ru/$CaCN_2$ catalytic system are summarized in Figure 6, where we used four Ru atoms per lateral cell to represent the effect of Ru on the surface structure. Here we considered a series of the Ru/$CaCN_2$ surface transformation upon its interaction with H_2 gas. We propose that Hydrogen interacts with the surface in three distinct modes, depending on its concentration. At low concentrations, H_2 binds to the Carbon atoms of the surface CN_2^{2-} ions and forms formally $[CN_2H_2]^{2-}$ species with ~0.7 eV gain per H_2 molecule. The formation of these C–H bonds weakens the C–N bonds, as manifested by increasing their bond lengths from ~1.33 Å to ~1.45 Å. For comparison, in the absence of Ru,

the C–N bond lengths are ~1.25 Å, i.e., the combined effect of the interaction with Ru and H_2 leads to their elongation by ~0.2 Å.

We propose that upon further exposure to H_2, its interaction with such elongated C–N bonds breaks them and leads to the formation of CNH_3 species, still bound to the surface, and Nitrogen atoms that remains bound to the Ru atoms, as shown in Figure 6c. The significant energy gain in this reaction (~0.9 eV per H atom) is in part due to stabilization of the Ru–N–Ru fragment, as evidenced by the Ru–N distances decreasing from ~1.98 Å to ~1.85 Å.

An additional H atom can displace the N atom from its site between the two Ru atoms into an adatom configuration shown. In our model, this step corresponds to the transition between configurations shown in Figure 6c and 6d. According to our calculations, this reaction is cost-neutral. Indeed, the number of Ru–N bonds is preserved in this process and the displacement of the neighboring Ru towards each other leads to the formation of an additional Ru–Ru bond which has a stabilizing effect. We note that in our model, the H atom adsorbed at this latter step adopts the charge state of H^- and occupies the site between the adsorbed Ru and the surface Ca^{2+} ions of the $CaCN_2$ surface; it is not visible in Figure 6d. Finally, we find that yet another H atom breaks another C–N bond and displaces the freed-up N atom to the adatom site, leading to the formation of an N_2 molecule (Figure 6e); the H remaining at the surface also occupies the site between the Ru and surface Ca^{2+} ions as an H^-. According to our calculations, this step is endothermic by ~1.2 eV. We note, however, that the reaction energy balance is dependent on the particular arrangement and concentration of the pre-adsorbed Ru atoms. Therefore, we interpret the calculated energy cost as an upper bound of the possible values.

Upon desorption of the N_2 molecule (0.3 eV activation energy) the surface contains CNH_n species (n = 2, 3), where N atoms are anchored to Ru atoms. These species react with Hydrogen in the same fashion as described above, with the energy gain of up to 0.5 eV per atom, except for the step leading to breaking C–N bond and the formation of CH_4 (Figure 6i) that is endothermic by ~0.65 eV. This cost is attributed to breaking one of the Ru–N bonds, as visible from the comparison of Figure 6h and 6i. It needs to be noted that the configuration shown in Figure 6i represents a metastable state. Indeed, desorption of CH_4 and relaxation of the Ru cluster into the configuration show in Figure 6j proceeds with the energy gain of over 1.1 eV, which suggests that concerted steps of C–N breaking and Ru–N–Ru relaxation are energetically favorable or, at least, cost neutral, similarly to what we found for the transition between configurations in Figure 6c and 6d.

Interestingly, and in agreement with the experimental data, we find that dissociated hydrogen species interaction with the Ru clusters can adopt two types of configurations: (i) they can bind to the surface Ru or (ii) to the Ca and Ru at the interface between the adsorbed Ru and the surface Ca^{2+} plane (see Figure 6), with the former configuration being only ~0.15 eV per H atom being thermodynamically preferred at 0 K. According to Bader population analysis, H species adopt a negative charge state H^{x-} (x ~0.3–0.4) in both cases but the overall charge is more negative at the Ca^{2+}/Ru interface. In other words, the presence of a Ca^{2+}/Ru and Ru/gas interfaces that can stabilize formally H^- and H^+ (in the presence of N) species, allow for a dynamic response of this system to the hydrogen chemical potential and prevents Ru poisoning.

To assess the kinetic factors associated with these transformations, we calculated energy barriers for the characteristic reaction steps shown in Figure 6. While the surface hydrogenation involves multiple steps, there are three steps that are key for this discussion: dissociative

adsorption of H_2 molecules resulting in the formation of CN_2H_2; desorption of molecular species, such as N_2, formed during this process; and a concerted process that involving splitting of the C–N bonds and expulsion of N into adatom configurations, including with formation of N_2 molecules, while their sites at the interface between Ca^{2+} ions and Ru are occupied by H^-. We also note that since the number of Ca–N bonds in our model is larger than that in other surface terminations detectable experimentally (see Supporting Information), calculated barriers for the latter processes are likely to be the upper bounds of those for the powder sample.

The calculated barriers and corresponding configurations are summarized in Figure 7. The H_2 dissociative attachment to the surface CN_2 proceeds with a calculated barrier of ~0.8 eV and overall energy gain of ~0.7 eV per H_2 molecule. The potential energy surface shown in Figure 7a includes displacement of H_2 as a whole towards the surface, followed by CI-NEB path containing 8 intermediate images. The barrier for desorption of N_2 molecules (Figure 7b) is ~0.5 eV, which is only slightly larger their binding energies (see Figure 6e,f). Other barriers we considered (Figure 7c) correspond to decomposition of CN_2H_2 anions resulting in the formation of surface N_2 molecules and incorporation of H^- ions at the interface between the Ru cluster and Ca^{2+} sublattice of $CaCN_2$. This concerted process involves several steps including H_2 dissociation, breaking the C–N bond and forming the C–H bond instead, and substituting the detached N with H^-. As a result, the N atom leaves its lattice site and stabilizes as a Ru adatom. Repeating this step produces enough N atoms on top of Ru clusters to create an N_2 molecule. The displacement of the N atoms to the adatom configurations allows for the formation of Ru–Ru bonds when these atoms are no longer separated by Nitrogens. This Ru reorganization, as well as the formation of N_2, provide exothermic contribution which makes the transition almost cost neutral (Figure 7c).

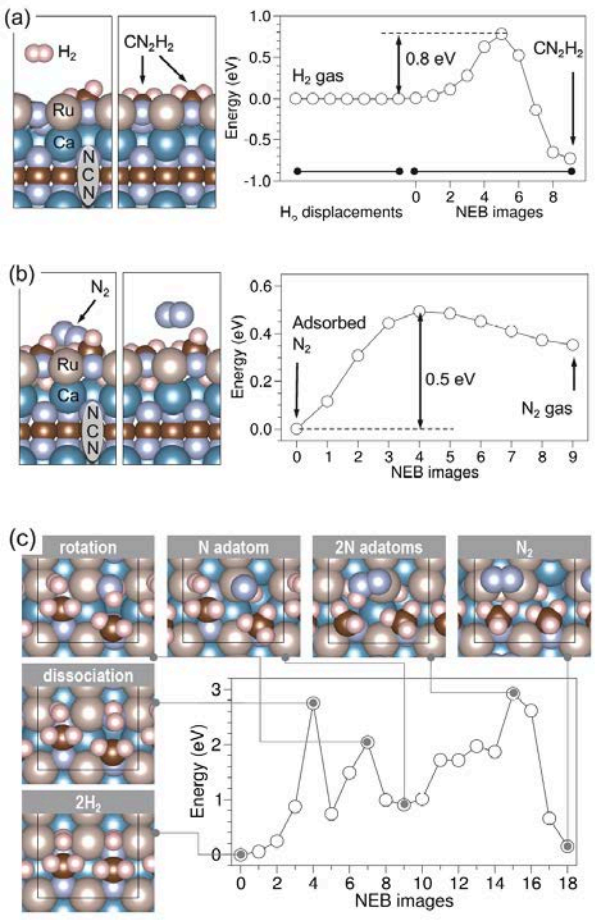

Figure 7. Local atomic structures and corresponding potential energy surfaces calculated for characteristic reactive steps in Figure 6. (a) Dissociative adsorption of H_2 leading to the formation of surface-bound CN_2H_2; (b) desorption of N_2; (c) H_2 dissociation resulting in the formation of N_2 molecules and incorporation of H^- species at the Ru/Ca^{2+} interface. Process in (c) involves several concerted steps including C-N → C-H bond switching.

To summarize, we propose that interaction of Ru/$CaCN_2$ with Hydrogen proceeds via a sequence of the following reactions steps: (i) conversion of CN_2 into CN_2H_2; (ii) breaking C–N

bonds with formation of CNH_3; (iii) displacement of N species from their original sites with the formation of H^- ions, N adatoms and N_2 molecules. These steps are accompanied by the formation and desorption of N_2 and CH_4 molecules. We emphasize that these reaction steps are also assisted by continuous rearrangement of the Ru species since the distribution of Ru atoms at the pristine surface is determined by their interactions with each other and with N atoms of the CN_2^{2-} ions. As CN_2^{2-} ions decompose and get substituted by H^- ions, the number and configurations of the Ru–N bonds changes and, therefore, the arrangement of the Ru atoms changes as well. Such dynamical behavior of the surface Ru provides a key contribution to the activation of the $Ru/CaCN_2$ surface.

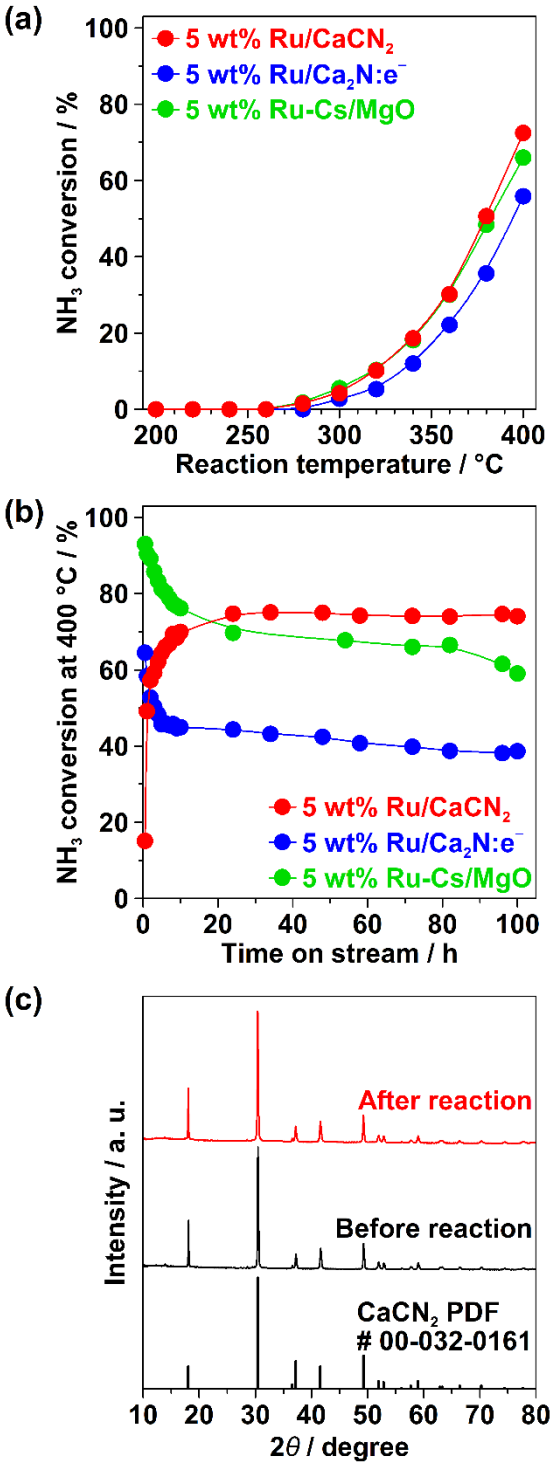

Figure 8. (a) Temperature dependence of the conversion in NH_3 decomposition over various supported Ru catalysts. These activities were investigated on samples after the catalytic reaction at 400 °C for 48 h at a WHSV of 15000 mL_{NH3} g_{cat}^{-1} h^{-1}. (b) Time courses of NH_3 decomposition

at 400 °C over various supported Ru catalysts (reaction conditions: catalyst 60 mg; NH_3 flow rate 15 mL min^{-1}; WHSV 15000 mL_{NH3} g_{cat}^{-1} h^{-1}). (c) XRD patterns of 5 wt% Ru/$CaCN_2$ before and after NH_3 decomposition at 400 °C for 100 h at a WHSV of 15000 mL_{NH3} g_{cat}^{-1} h^{-1} and reference XRD pattern of $CaCN_2$.

Table 2. Catalytic properties of supported Ru nanoparticles (NPs) in NH_3 decomposition reaction as a function of support.

Catalyst	NH_3 conversion[a] / %	Decomposition rate of NH_3[a] / kg_{NH3} kg_{cat}^{-1} h^{-1}	TOF[a] / s^{-1}	E_a[ac] / kJ mol^{-1}
5 wt% Ru/$CaCN_2$	72.5	7.5	0.9[b]	85.2
5 wt% Ru/Ca_2N:e^-	55.9	5.9	1.0[b]	112
5 wt% Ru-Cs/MgO	66.0	6.9	0.5[b]	83.2
5 wt% Ru/MgO	36.5	3.8	-	-
5 wt% Ru/γ-Al_2O_3	27.8	2.9	-	-

[a]These activities were investigated on samples after the catalytic reaction at 400 °C for 48 h at a WHSV of 15000 mL_{NH3} g_{cat}^{-1} h^{-1}. Reaction conditions: catalyst 60 mg; temperature 400 °C; NH_3 gas 15 mL min^{-1}; 15000 mL_{NH3} g_{cat}^{-1} h^{-1}; pressure 0.1 MPa. [b]These values were estimated by averaging the particle sizes measured by STEM. [c]The apparent activation energy E_a was calculated from Arrhenius plots for the decomposition rate of NH_3 in the temperature range of 320–360 °C.

The catalytic performance of Ru/$CaCN_2$ for NH_3 decomposition was also evaluated. Figure 8a shows temperature dependence on NH_3 conversion of Ru/$CaCN_2$, Ru/Ca_2N:e^- and Ru-Cs/MgO in NH_3 decomposition. The temperature dependence was measured using catalysts after 48 h of the reaction at 400 °C. The NH_3 conversion of Ru/$CaCN_2$ was higher than those of Ru/Ca_2N:e^- and comparable to that of Ru-Cs/MgO over the entire temperature range tested. Figure 8b shows

time courses of NH_3 decomposition at 400 °C over Ru/$CaCN_2$, Ru/Ca_2N:e^- and Ru-Cs/MgO. The activity of Ru/$CaCN_2$ drastically elevated in the early stages of the reaction and then plateaued. As shown in Figure 8c, there is no change in the XRD pattern of Ru/$CaCN_2$ before and after the stability test. In contrast, the activities of Ru/Ca_2N:e^- and Ru-Cs/MgO dropped significantly in the initial 10 hours and continuously decreased with reaction time after 10 hours. Table 2 summarizes catalytic properties of various Ru catalysts for NH_3 decomposition at 400 °C. For Ru/$CaCN_2$, Ru/Ca_2N:e^- and Ru-Cs/MgO, the properties after 48 h of the reaction are shown. There were two classes of the level of activities of the catalysts tested. The NH_3 conversion and decomposition rate of NH_3 for Ru/$CaCN_2$ were at the same level of those of Ru/Ca_2N:e^- and Ru-Cs/MgO and, over 2-fold higher than those of Ru/MgO and Ru/γ-Al_2O_3. While the $CaCN_2$ is not an electride material as such, it has a strong electronic promotion effect for Ru catalyst that is critical for NH_3 decomposition. The surface CN_2 vacancies at the Ru/support interface may account for the strong electronic promotion ability. The H_2-TPD of Ru/$CaCN_2$ after NH_3 decomposition (Figure S9) showed similar H_2 desorption profile as the case of NH_3 synthesis (Figure S8), whereas no NH_3 was desorbed from the catalyst. In addition, the amount of H_2 desorption is determined to be 0.20 mmol g_{cat}^{-1}, which is similar level of that for Ru/$CaCN_2$ after NH_3 synthesis. This result suggests that H^- ions rather than NH_x species occupy the CN_2 vacancy sites on the $CaCN_2$ surface during NH_3 decomposition and the surface composition of Ru/$CaCN_2$ are similar between NH_3 synthesis and decomposition. The TOF with Ru/$CaCN_2$ for NH_3 decomposition was identical to that with Ru/Ca_2N:e^- and twice as high as that with Ru-Cs/MgO. The E_a of each catalyst for NH_3 decomposition was very similar to the conventional Ru catalysts reported to date (Table 2 and Figure S10). This suggests that the reaction mechanism of NH_3 decomposition over Ru/$CaCN_2$ is same as that of conventional Ru catalysts, in which the

recombination of nitrogen adatoms is the rate-determining step.[53] In view of the NH_3 conversion, TOF and stability, Ru/$CaCN_2$ can be regarded as a promising catalyst not only for NH_3 synthesis but also for NH_3 decomposition.

CONCLUSIONS

We investigated an air-stable ionic compound, $CaCN_2$, as a catalytic support for NH_3 synthesis and decomposition. Ru/$CaCN_2$ exhibited more efficient and consistent performances under low temperature conditions than electride-supported and alkali-promoted oxide-supported Ru catalysts in both reactions. From the results of H_2-TPR, TPD and DFT calculation, it was considered that quasi-electride structure is formed at CN_2 vacancies on the surface during the catalytic reaction, which accounts for the low work function and hydrogen storage capability. The present findings reveal that ionic compounds, which are not intrinsically low work function materials, are converted into quasi-electride materials via the formation of anion vacancies and have a great potential to function as efficient catalyst support for NH_3 synthesis and decomposition.

ASSOCIATED CONTENT

Supporting Information.

The following files are available free of charge via the Internet at http://pubs.acs.org.

Supporting method for preparation of reference Ru catalysts and calculations, XRD patterns of $Ru/CaCN_2$ without exposure to air before and after NH_3 synthesis, HAADF-STEM image of $Ru/Ca_2N{:}e^-$ after NH_3 synthesis, Arrhenius plots of NH_3 synthesis and decomposition for various supported Ru catalysts, catalytic performance on reported catalysts for NH_3 synthesis under similar conditions, kinetic analysis for NH_3 synthesis over $Ru/CaCN_2$, H_2-TPD profile for $Ru/CaCN_2$ after NH_3 synthesis and decomposition.

AUTHOR INFORMATION

Corresponding Author

* E-mail: kitano.m.aa@m.titech.ac.jp

* E-mail: hosono@msl.titech.ac.jp

Notes

The authors declare no competing financial interest.

ACKNOWLEDGMENT

The authors thank N. Makino and E. Fujita for experimental support. This work was supported by PRESTO Grant (No. JPMJPR18T6) from the Japan Science and Technology Agency (JST) and Kakenhi Grants-in-Aid (Nos. JP19H05051, JP19H02512 and 17H06153) from the Japan Society for the Promotion of Science (JSPS). A part of this work was supported by Tokuyama Science Foundation. The XAFS measurements were conducted under the approval of PF-PAC No. 2013S2-002. PVS was supported by the Laboratory Directed Research and Development

program at Pacific Northwest National Laboratory (PNNL). PNNL is a multiprogram national laboratory operated by Battelle for the DOE under Contract DEAC05-76RL01830.

REFERENCES

(1) Klerke, A.; Christensen, C. H.; Nørskov, J. K.; Vegge, T. Ammonia for hydrogen storage: challenges and opportunities. *J. Mater. Chem.* **2008**, *18*, 2304–2310.

(2) Wickramasinghe, L. A.; Ogawa, T.; Schrock, R. R.; Muller, P. Reduction of Dinitrogen to Ammonia Catalyzed by Molybdenum Diamido Complexes. *J. Am. Chem. Soc.* **2017**, *139*, 9132–9135.

(3) Shima, T.; Luo, G.; Hu, S.; Luo, Y.; Hou, Z. Experimental and Computational Studies of Dinitrogen Activation and Hydrogenation at a Tetranuclear Titanium Imide/Hydride Framework. *J. Am. Chem. Soc.* **2019**, *141*, 2713–2720.

(4) Ashida, Y.; Arashiba, K.; Nakajima, K.; Nishibayashi, Y. Molybdenum-catalysed ammonia production with samarium diiodide and alcohols or water. *Nature* **2019**, *568*, 536–540.

(5) van der Ham, C. J. M.; Koper, M. T. M.; Hetterscheid, D. G. H. Challenges in reduction of dinitrogen by proton and electron transfer. *Chem. Soc. Rev.* **2014**, *43*, 5183–5191.

(6) Chu, K.; Li, Q.-q.; Liu, Y.-p.; Wang, J.; Cheng, Y.-h. Filling the nitrogen vacancies with sulphur dopants in graphitic C_3N_4 for efficient and robust electrocatalytic nitrogen reduction. *Appl. Catal., B* **2020**, *267*, 118693.

(7) Chu, K.; Liu, Y.-p.; Li, Y.-b.; Guo, Y.-l.; Tian, Y. Two-dimensional (2D)/2D Interface Engineering of a MoS_2/C_3N_4 Heterostructure for Promoted Electrocatalytic Nitrogen Fixation. *ACS Appl. Mater. Interfaces* **2020**, *12*, 7081–7090.

(8) Chu, K.; Liu, Y.-p.; Li, Y.-b.; Guo, Y.-l.; Tian, Y.; Zhang, H. Multi-functional Mo-doping in MnO_2 nanoflowers toward efficient and robust electrocatalytic nitrogen fixation. *Appl. Catal. B: Environmental* **2020**, *264*, 118525.

(9) Iwamoto, M.; Akiyama, M.; Aihara, K.; Deguchi, T. Ammonia Synthesis on Wool-Like Au, Pt, Pd, Ag, or Cu Electrode Catalysts in Nonthermal Atmospheric-Pressure Plasma of N_2 and H_2. *ACS Catal.* **2017**, *7*, 6924–6929.

(10) Boisen, A.; Dahl, S.; Nørskov, J. K.; Christensen, C. H. Why the optimal ammonia synthesis catalyst is not the optimal ammonia decomposition catalyst. *J. Catal.* **2005**, *230*, 309–312.

(11) Hansgen, D. A.; Vlachos, D. G.; Chen, J. G. Using first principles to predict bimetallic catalysts for the ammonia decomposition reaction. *Nat. Chem.* **2010**, *2*, 484–489.

(12) Aika, K.; Takano, T.; Murata, S. Preparation and Characterization of Chlorine-Free Ruthenium Catalysts and the Promoter Effect in Ammonia Synthesis. 3. A Magnesia-Supported Ruthenium Catalyst. *J. Catal.* **1992**, *136*, 126–140.

(13) Yin, S. F.; Xu, B. Q.; Zhou, X. P.; Au, C. T. A mini-review on ammonia decomposition catalysts for on-site generation of hydrogen for fuel cell applications. *Appl. Catal., A* **2004**, *277*, 1–9.

(14) Gambarotta, S.; Scott, J. Multimetallic Cooperative Activation of N_2. *Angew. Chem. Int. Ed.* **2004**, *43*, 5298–5308.

(15) Tsai, W.; Weinberg, W. H. Steady-State Decomposition of Ammonia on the Ru(001) Surface. *J. Phys. Chem.* **1987**, *91*, 5302–5307.

(16) Aika, K.; Hori, H.; Ozaki, A. Activation of nitrogen by alkali metal promoted transition metal. I. Ammonia synthesis over ruthenium promoted by alkali metal. *J. Catal.* **1972**, *27*, 424–431.

(17) Bielawa, H.; Hinrichsen, O.; Birkner, A.; Muhler, M. The Ammonia-Synthesis Catalyst of the Next Generation: Barium-Promoted Oxide-Supported Ruthenium. *Angew. Chem. Int. Ed.* **2001**, *40*, 1061–1063.

(18) Ertl, G. Reactions at surfaces: from atoms to complexity (Nobel lecture). *Angew. Chem. Int. Ed.* **2008**, *47*, 3524–3535.

(19) Sato, K.; Miyahara, S.-i.; Ogura, Y.; Tsujimaru, K.; Wada, Y.; Toriyama, T.; Yamamoto, T.; Matsumura, S.; Nagaoka, K. Surface Dynamics for Creating Highly Active Ru Sites for Ammonia Synthesis: Accumulation of a Low-Crystalline, Oxygen-Deficient Nanofraction. *ACS Sustainable Chem. Eng.* **2020**, *8*, 2726–2734.

(20) Rarog-Pilecka, W.; Szmigiel, D.; Kowalczyk, Z.; Jodzis, S.; Zielinski, J. Ammonia decomposition over the carbon-based ruthenium catalyst promoted with barium or cesium. *J. Catal.* **2003**, *218*, 465–469.

(21) Yin, S.-F.; Xu, B.-Q.; Wang, S.-J.; Au, C.-T. Nanosized Ru on high-surface-area superbasic ZrO_2-KOH for efficient generation of hydrogen via ammonia decomposition. *Appl. Catal., A* **2006**, *301*, 202–210.

(22) Nagaoka, K.; Honda, K.; Ibuki, M.; Sato, K.; Takita, Y. Highly active $Cs_2O/Ru/Pr_6O_{11}$ as a catalyst for ammonia decomposition. *Chem. Lett.* **2010**, *39*, 918–919.

(23) Ozaki, A. Development of alkali-promoted ruthenium as a novel catalyst for ammonia synthesis. *Acc. Chem. Res.* **1981**, *14*, 16–21.

(24) Rao, C. N. R.; Rao, G. R. Nature of nitrogen adsorbed on transition metal surfaces as revealed by electron spectroscopy and cognate techniques. *Surf. Sci. Rep.* **1991**, *13*, 221–263.

(25) Kitano, M.; Inoue, Y.; Yamazaki, Y.; Hayashi, F.; Kanbara, S.; Matsuishi, S.; Yokoyama, T.; Kim, S.-W.; Hara, M.; Hosono, H. Ammonia synthesis using a stable electride as an electron donor and reversible hydrogen store. *Nat. Chem.* **2012**, *4*, 934–940.

(26) Hayashi, F.; Toda, Y.; Kanie, Y.; Kitano, M.; Inoue, Y.; Yokoyama, T.; Hara, M.; Hosono, H. Ammonia decomposition by ruthenium nanoparticles loaded on inorganic electride C12A7:e^-. *Chem. Sci.* **2013**, *4*, 3124–3130.

(27) Matsuishi, S.; Toda, Y.; Miyakawa, M.; Hayashi, K.; Kamiya, T.; Hirano, M.; Tanaka, I.; Hosono, H. High-Density Electron Anions in a Nanoporous Single Crystal: $[Ca_{24}Al_{28}O_{64}]^{4+}(4e^-)$. *Science* **2003**, *301*, 626–630.

(28) Kitano, M.; Inoue, Y.; Ishikawa, H.; Yamagata, K.; Nakao, T.; Tada, T.; Matsuishi, S.; Yokoyama, T.; Hara, M.; Hosono, H. Essential role of hydride ion in ruthenium-based ammonia synthesis catalysts. *Chem. Sci.* **2016**, *7*, 4036–4043.

(29) Ong, P.-V.; Johnson, L. E.; Hosono, H.; Sushko, P. V. Structure and stability of CaH_2 surfaces: on the possibility of electron-rich surfaces in metal hydrides for catalysis. *J. Mater. Chem. A* **2017**, *5*, 5550–5558.

(30) Inoue, Y.; Kitano, M.; Kishida, K.; Abe, H.; Niwa, Y.; Sasase, M.; Fujita, Y.; Ishikawa, H.; Yokoyama, T.; Hara, M.; Hosono, H. Efficient and Stable Ammonia Synthesis by Self-Organized Flat Ru Nanoparticles on Calcium Amide. *ACS Catal.* **2016**, *6*, 7577–7584.

(31) Kitano, M.; Inoue, Y.; Sasase, M.; Kishida, K.; Kobayashi, Y.; Nishiyama, K.; Tada, T.; Kawamura, S.; Yokoyama, T.; Hara, M.; Hosono, H. Self-organized Ruthenium-Barium Core-Shell Nanoparticles on a Mesoporous Calcium Amide Matrix for Efficient Low-Temperature Ammonia Synthesis. *Angew. Chem. Int. Ed.* **2018**, *57*, 2648–2652.

(32) Momma, K.; Izumi, F. VESTA 3 for three-dimensional visualization of crystal, volumetric and morphology data. *J. Appl. Crystallogr.* **2011**, *44*, 1272–1276.

(33) Lee, K.; Kim, S. W.; Toda, Y.; Matsuishi, S.; Hosono, H. Dicalcium nitride as a two-dimensional electride with an anionic electron layer. *Nature* **2013**, *494*, 336–340.

(34) Kojima, R.; Aika, K.-i. Cobalt molybdenum bimetallic nitride catalysts for ammonia synthesis. Part 2. Kinetic study. *Appl. Catal., A* **2001**, *218*, 121–128.

(35) Levenspiel, O. *Chemical Reaction Engineering*, 3rd ed.; Wiley-VCH Verlag GmbH & Co. KGaA: New York, 1998; p 87.

(36) Bergeret, G.; Gallezot, P. In *Handbook of Heterogeneous Catalysis*; Ertl, G.; Knöezinger, H.; Schüeth, F.; Weitkamp, J., Eds.; Wiley-VCH Verlag GmbH & Co. KGaA: Weinheim, Germany, 2008; p 757.

(37) Ravel, B.; Newville, M. ATHENA, ARTEMIS, HEPHAESTUS: data analysis for x-ray absorption spectroscopy using IFEFFIT. *J. Synchrotron Rad.* **2005**, *12*, 537–541.

(38) Zabinsky, S. I.; Rehr, J. J.; Aukudinov, A.; Albers, R. C.; Eller, M. J. Multiple-scattering calculations of x-ray-absorption spectra. *Phys. Rev. B* **1995**, *52*, 2995–3009.

(39) Kresse, G.; Hafner, J. Ab initio molecular-dynamics simulation of the liquid-metal-amorphous-semiconductor transition in germanium. *Phys. Rev. B* **1994**, *49*, 14251–14269.

(40) Kresse, G.; Furthmüller, J. Efficient iterative schemes for ab initio total-energy calculations using a plane-wave basis set. *Phys. Rev. B* **1996**, *54*, 11169–11186.

(41) Blöchl, P. E. Projector augmented-wave method. *Phys. Rev. B* **1994**, *50*, 17953–17979.

(42) Perdew, J. P.; Ruzsinszky, A.; Csonka, G. I.; Vydrov, O. A.; Scuseria, G. E.; Constantin, L. A.; Zhou, X.; Burke, K. Restoring the Density-Gradient Expansion for Exchange in Solids and Surfaces. *Phys. Rev. Lett.* **2008**, *100*, 136406/1–136406/4.

(43) Jacobsen, C. J. H.; Dahl, S.; Hansen, P. L.; Törnqvist, E.; Jensen, L.; Topsøe, H.; Prip, D. V.; Møenshaug, P. B.; Chorkendorff, I. Structure sensitivity of supported ruthenium catalysts for ammonia synthesis. *J. Mol. Catal. A: Chem.* **2000**, *163*, 19–26.

(44) Kishida, K.; Kitano, M.; Inoue, Y.; Sasase, M.; Nakao, T.; Tada, T.; Abe, H.; Niwa, Y.; Yokoyama, T.; Hara, M.; Hosono, H. Large Oblate Hemispheroidal Ruthenium Particles Supported on Calcium Amide as Efficient Catalysts for Ammonia Decomposition. *Chem. Eur. J.* **2018**, *24*, 7976–7984.

(45) Lu, Y.; Li, J.; Tada, T.; Toda, Y.; Ueda, S.; Yokoyama, T.; Kitano, M.; Hosono, H. Water Durable Electride Y_5Si_3: Electronic Structure and Catalytic Activity for Ammonia Synthesis. *J. Am. Chem. Soc.* **2016**, *138*, 3970–3973.

(46) Mizoguchi, H.; Okunaka, M.; Kitano, M.; Matsuishi, S.; Yokoyama, T.; Hosono, H. Hydride-Based Electride Material, LnH_2 (Ln = La, Ce, or Y). *Inorg. Chem.* **2016**, *55*, 8833–8838.

(47) Wu, J.; Gong, Y.; Inoshita, T.; Fredrickson, D. C.; Wang, J.; Lu, Y.; Kitano, M.; Hosono, H. Tiered Electron Anions in Multiple Voids of LaScSi and Their Applications to Ammonia Synthesis. *Adv. Mater.* **2017**, *29*, 1700926.

(48) Mizoguchi, H.; Park, S.-W.; Kishida, K.; Kitano, M.; Kim, J.; Sasase, M.; Honda, T.; Ikeda, K.; Otomo, T.; Hosono, H. Zeolitic Intermetallics: LnNiSi (Ln = La–Nd). *J. Am. Chem. Soc.* **2019**, *141*, 3376–3379.

(49) Wu, J.; Li, J.; Gong, Y.; Kitano, M.; Inoshita, T.; Hosono, H. Intermetallic Electride Catalyst as a Platform for Ammonia Synthesis. *Angew. Chem. Int. Ed.* **2019**, *58*, 825–829.

(50) Rosowski, F.; Hornung, A.; Hinrichsen, O.; Herein, D.; Muhler, M.; Ertl, G. Ruthenium catalysts for ammonia synthesis at high pressures: Preparation, characterization, and power-law kinetics. *Appl. Catal., A* **1997**, *151*, 443–460.

(51) Kitano, M.; Kanbara, S.; Inoue, Y.; Kuganathan, N.; Sushko, P. V.; Yokoyama, T.; Hara, M.; Hosono, H. Electride support boosts nitrogen dissociation over ruthenium catalyst and shifts the bottleneck in ammonia synthesis. *Nat. Commun.* **2015**, *6*, 6731.

(52) Kitano, M.; Kujirai, J.; Ogasawara, K.; Matsuishi, S.; Tada, T.; Abe, H.; Niwa, Y.; Hosono, H. Low-Temperature Synthesis of Perovskite Oxynitride-Hydrides as Ammonia Synthesis Catalysts. *J. Am. Chem. Soc.* **2019**, *141*, 20344–20353.

(53) Temkin, M. I.; Pyzhev, V. Kinetics of ammonia synthesis on promoted iron catalysts. *Acta Physicochim. URSS* **1940**, *12*, 327–356.

TOC